Carbon Dots/$NiCo_2O_4$ Nanocomposites with Various Morphologies for High Performance Supercapacitors

Ji-Shi Wei, Hui Ding, Peng Zhang, Yan-Fang Song, Jie Chen, Yong-Gang Wang, and Huan-Ming Xiong**

Carbon dots (CDs), as a new class of 0D carbon nanomaterials, have become a focus in fundamental researches due to their unique properties in both physics and chemistry. They also attract the attention of engineers because they show high yield in fabrication, good dispersion in solvents, and low cost for production.[1–4] By far, CDs were mainly studied for bioimaging probes, fluorescence sensors, photovoltaic devices, and light-emitting diodes,[5,6] while their applications in the electrode materials[7,8] were rarely reported. Nevertheless, several pioneer researches have shown the promising future of CDs as electrode materials for supercapacitor, like the CDs/RuO_2,[1] CDs//PANI,[4] and CDs-graphene composites.[9] It has been found that CDs can provide an excellent interface for the interactions between electrolytes and electrodes, so as to improve the specific capacitance, the rate performance, and the cycling stability.[8,10]

It is well known that the common advantages of the typical supercapacitor electrode materials include high power density, excellent coulomb efficiency, low maintenance cost, and long lifespan.[11,12] But in comparison with those battery electrode materials,[13,14] the supercapacitor electrode materials always fail in the lower energy density because their energy storage is limited on the electrode surfaces in form of the double layer capacitance. Simon and co-workers and Gogotsi and co-workers pointed out that an electrode material with high energy density should possess abundant reversible redox reactions,[15,16] as well as a good electronic conductivity. Recently, the mixed transition metal oxides (MTMOs),[17] like $NiCo_2O_4$,[18,19] have been investigated intensively for supercapacitors. Their high energy densities are based on the metal valence variations during redox reactions, but some natural deficiencies like the lower electronic conductivities and the volume change effect always render the short life cycles and the poor rate performances. To overcome these shortcomings, graphene oxide,[20] carbon nanotubes (CNTs),[21] and active carbon[22] have been employed to increase the surface area, the surface wettability, and conductivity of MTMOs. In fact, the incorporation of carbon materials can only resolve the above problems partially, and it even brings about other disadvantages. For instance, not all the carbon components make the positive contribution to the whole electrochemical properties. A dense carbon coating will hinder the reactions between metal oxide particles and electrolyte. And too much carbon component will decrease the specific capacitance in the whole,[21,22] because carbon materials have very small capacitances themselves. In addition, some carbon materials like graphene and CNTs, are so expensive that they increase the cost of MTMOs-carbon composites.

However, there will be a large space for improvement of the MTMOs-carbon materials when CDs are employed, because CDs are 0D nanoparticles with natural merits over the other counterparts. First of all, CDs are much more flexible for constructing various structures than those multidimensional carbon materials. Second, when CDs and MTMOs assemble together, there will be more interspaces and pathways for both ions transfer and volume change. Most importantly, CDs have the highest specific surface areas when their diameters are 1–2 nm, that means they can carry more organic groups for surface wettability, form larger interface areas between CDs, MTMOs, and electrolytes for electrochemical reactions. And a good particle distribution of CDs will provide uniform surface states for stable cycling performances. Finally, CDs are apt to be doped by many elements, like N, O, S, P, etc.,[5–7] so their physicochemical properties can be tuned optionally to meet the requirement of electrodes. All these merits guarantee a promising future of CDs-MTMOs composites with respects to the electrochemical energy storage. In addition, the production cost and the process complexity of CDs are much lower than both carbon nanotubes and graphene derivatives.[5–7,14,23]

In the present work, we used a facile hydrothermal route to synthesize N-doped CDs with high graphitization degrees and employed them to prepare the CDs/$NiCo_2O_4$ nanocomposites. Interestingly, multistructures of the composites could be achieved by adjusting the inventory rating of CDs in reactions, from sea urchin to flower and even bayberry. In comparison with the hard template method, soft template method, chemical deposition method, and other complicated ways in literature, our route is a cheap, facile, and

J.-S. Wei, Dr. H. Ding, P. Zhang, Dr. Y.-F. Song, J. Chen, Prof. Y.-G. Wang, Prof. H.-M. Xiong
Department of Chemistry and Laboratory of Advanced Materials
Fudan University
Shanghai 200433, P. R. China
E-mail: ygwang@fudan.edu.cn; hmxiong@fudan.edu.cn

DOI: 10.1002/smll.201602164

efficient way to build up multimorphologies. The optimal sample exhibited a specific capacitance of 2168 F g^{-1} at a current density of 1 A g^{-1}. When the current density varied from 1 to 30 A g^{-1}, the retention rate of this sample reached 75.2%, which is far beyond the data of $NiCo_2O_4$ single crystal.[24] This sample was employed as the positive electrode to fabricate a hybrid supercapacitor, with hierarchical porous carbon (HPC) as the negative electrode. Such hybrid supercapacitor exhibited a high specific capacitance of 138.8 F g^{-1}, corresponding to a high energy density of 62.0 Wh kg^{-1}. Moreover, this hybrid device showed 99.96% capacity retention rate after 5000 cycles at a high current density of 30 A g^{-1}. Compared with the hybrid supercapacitors reported recently, in which the negative electrodes are porous carbon based materials and the positive electrodes are $NiCo_2O_4$ composite with carbon nanotubes,[21] Au nanotubes,[25] or MnO_2,[26] our present hybrid capacitor showed remarkable improvement in cycling stability, energy density, and power density. These excellent performances result from the suitable surface states, low electrochemical impedances, and the unique nanostructures of our CDs/$NiCo_2O_4$ composites, as proved by the following experiments.

Experimentally, CDs were synthesized by treating citric acid (CA), ethylene diamine (EDA), and phosphorus oxide (P_2O_5) together in autoclaves hydrothermally, and then washed by ethanol (see the Supporting Information). The as-prepared CDs are characterized by TEM (Transmission Electron Microscopy) that shows the products are uniform and monodispersed with diameters of 2–4 nm (**Scheme 1**A). The corresponding HRTEM (High Resolution TEM) image (Scheme 1B) exhibits a clear fringe distance of 0.34 nm, close to the (002) crystal lattice distance of graphite,[1,2] indicating that the product has a high degree of graphitization. The UV–vis absorption curve of the CDs contains two typical absorption bands at 245 and 348 nm, corresponding to the electron transitions from the π (or n) orbital to the π^* orbital of the C=C and C=O bonds, respectively (Figure S1, Supporting Information). The photoluminescence spectra of the CDs exhibit a broad peak at around 468 nm under an excitation light of 365 nm. These optical features confirm that the as-prepared CDs are similar to those typical CDs in our previous works.[27–29]

Scheme 1 illustrates the synthetic routes and the products with different morphologies. These products are denoted as NCO-*X*, in which NCO represents the $NiCo_2O_4$ while *X* represents the concentration (mg mL^{-1}) of CDs in the reaction. The morphologies of products depend on the amount of CDs in synthesis. Four typical samples are investigated by FESEM (Field Emission Scanning Electron Microscopy, Scheme 1 C–F and Figure S2 (Supporting Information)), and the results show that they are generally uniform spheres with diameters of 2.5–5.0 μm but have different surface structures. When no CDs were incorporated, the NCO-0 spheres had nanoneedles with diameters of 150–180 nm on surfaces, just like sea urchins. A small amount of CDs (0.25 mg mL^{-1}) added in synthesis reduce the length of nanoneedles to 70–80 nm, and the obtained NCO-0.25 looks like chestnut. When more CDs (0.5 mg mL^{-1}) are added during synthesis, these nanoneedles disappear and the CDs/$NiCo_2O_4$ morphology turns to be flower dramatically! The intertwined nanopetals of such NCO-0.5 have a thickness of 20–30 nm, which change to be numerous ca. 30 nm sized nanodots when the amount of CDs is increased to 1.0 mg mL^{-1}, so the resulting NCO-1 looks like bayberry finally. The morphological variations result in the different specific surface areas (SSAs) of the products. Nitrogen adsorption measurements show that the flower NCO-0.5 has the largest SSA of 158.66 m^2 g^{-1}. And the SSAs of the chestnut NCO-0.25, the bayberry NCO-1, and

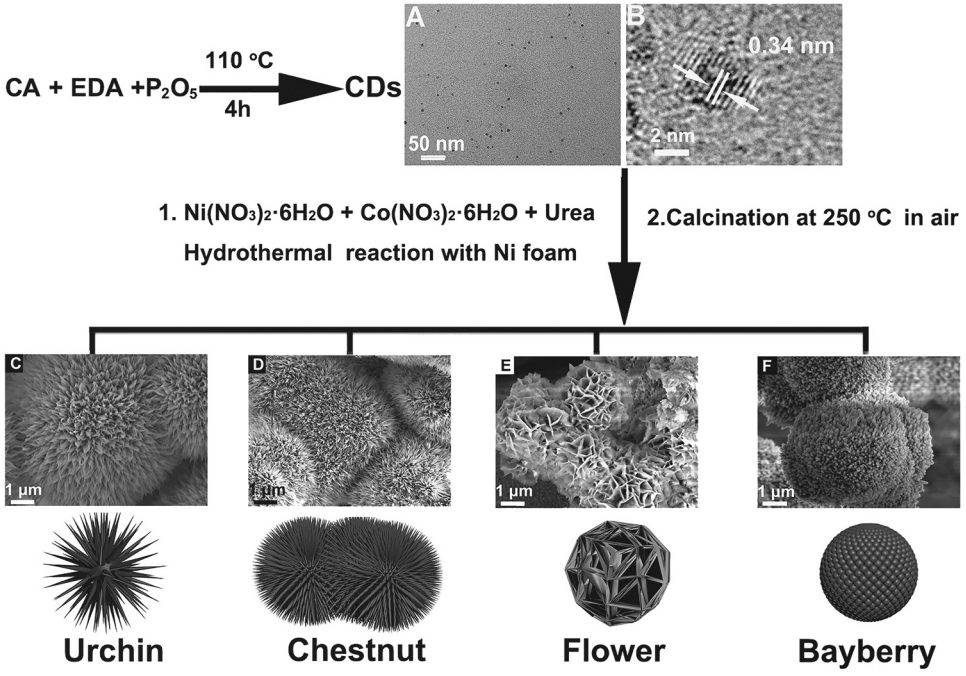

Scheme 1. A,B) The CDs are synthesized hydrothermally with uniform sizes and employed to prepare C–F) the CDs/$NiCo_2O_4$ composites with different morphologies.

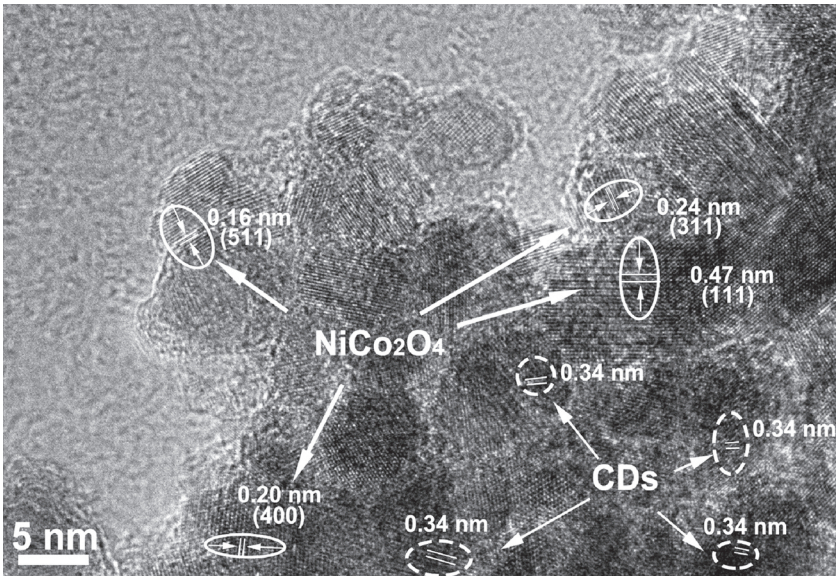

Figure 1. HRTEM image of the CDs/$NiCo_2O_4$ composite (NCO-0.5) in which the $NiCo_2O_4$ particles and CDs are marked by white circles, respectively.

the sea-urchin NCO-0 are 123.39, 104.42, and 89.67 $m^2\ g^{-1}$, respectively.

The HRTEM image (**Figure 1**) of the flower CD/$NiCo_2O_4$ composite (NCO-0.5) shows that the CDs are evenly combined with $NiCo_2O_4$ particles to form the petal structure. It is clear that not only the surface plates but also the internal spheres are constructed by nanoparticles. But the CDs with graphitized lattice are mainly observed at the edge of the composite, indicating that CDs mainly locate on the surface of the composite and fill in the gaps between $NiCo_2O_4$ nanoparticles. Such structure will make CDs contact with the electrolyte sufficiently when they are fabricated as the electrode materials, and the functional groups on CDs will contribute to the pseudocapacitance and facilitate the fast transfer of charge carriers during the charge–discharge processes.[1,2]

The compositions and structures of products are characterized by FTIR (Fourier Transform Infrared Spectroscopy), XRD (X-Ray Diffraction), and XPS (X-ray Photoelectron Spectroscopy) measurements, respectively. The FTIR spectra of CDs and CDs/$NiCo_2O_4$ composites are compared in Figure S3 (Supporting Information). For CDs, three bands at 3450, 1721, and 1630 cm^{-1} correspond to the O−H/N−H, C=O, and C=N stretching vibrations,[27,30,31] respectively. Another broad band within 1000–1200 cm^{-1} contains the stretching vibrations of C−O (ca. 1040 cm^{-1}), P−O (ca. 1050 cm^{-1}), and C−N (ca. 1170 cm^{-1}).[31,32] In addition, the starting material P_2O_5 brings new functional groups to CDs, like P−H vibrations at 2350 cm^{-1} and P−O vibrations at 1050 cm^{-1}.[32] In comparison with the spectra of CDs, the FTIR results of CDs/$NiCo_2O_4$ composites exhibit two significant differences. One is 1380 cm^{-1}, attributed to the asymmetric stretching vibrations of Td−O−Oh. Td−O−Oh is the oxygen-containing chemical bond connecting the tetrahedron and the octahedron structures of $NiCo_2O_4$ lattice.[33] The other is the typical metal-oxygen vibrations of $NiCo_2O_4$ at 650 and 560 cm^{-1}, respectively.[34] Therefore, the FTIR data prove that CDs and $NiCo_2O_4$ have formed complexes, which ensures the structural stability of CDs/$NiCo_2O_4$ on one hand, and on the other, facilitates the charge transfer between CDs and $NiCo_2O_4$ nanoparticles. Based on the above results, we can speculate the formation mechanism for the different morphologies of the products. When $NiCo_2O_4$ nanoparticles form in the hydrothermal system, they prefer to be spheres at the beginning.[35] But the electronic structure difference between Co^{2+} ions (octahedral coordination) and Ni^{2+} ions (square-planar coordination) renders the crystal growth along the *c*-axis of the bimetallic (Ni, Co) carbonate hydroxide, leading to the formation of nanoneedles on $NiCo_2O_4$ sphere surfaces.[36] However, when CDs are incorporated in the reaction, they will coat on the newly formed $NiCo_2O_4$ spheres due to the coordination effects. The higher the concentration of CDs, the heavier is the prevention on the anisotropic growth of $NiCo_2O_4$, and finally the nanoneedles are reduced to nanodots.[37]

In the XRD patterns of these samples, all of the diffraction peaks at 18.9°, 31.3°, 36.7°, 44.5°, 59.0°, and 64.9° are indexed as the (111), (220), (311), (400), (511), and (440) crystal planes of $NiCo_2O_4$,[38,39] respectively, in accord with the JCPDS No. 20-0781 (a_0 = 8.110 Å). There are no obvious peaks assigned to CDs, because the crystallinity of CDs is relatively low. To obtain more information about the surface structures of CDs/$NiCo_2O_4$, NCO-0.5 is investigated by XPS measurements as shown in Figure S5 (Supporting Information). The full XPS spectra in Figure S5A (Supporting Information) confirm the presence of Ni, Co, O, C, and N in NCO-0.5. The Ni 2p spectrum (Figure S5B, Supporting Information) is composed of two spin-orbit doublets and two shake-up satellites,[20] confirming the presence of both Ni (II) and Ni (III) ions. In detail, the fitting peaks of binding energies at 856.5 and 873.7 eV are ascribed to Ni (II), while the peaks at 858.5 and 875.5 eV are ascribed to Ni (III), respectively.[20,40] Similarly, the fitted result of Co 2p is shown in Figure S5C (Supporting Information), which shows the Co (III) peaks at 781.1 and 797.1 eV, and the Co (II) peaks at 782.1 and 799.1 eV, respectively.[41] The high-resolution O 1s spectrum in Figure S5D (Supporting Information) can be deconvoluted into four different peaks, denoted as O1, O2, O3, and O4, respectively. The O1 peak at 528.9 eV indicates the typical metal-oxygen bonds. The O2 peak at 530.9 eV represents the oxygen in hydroxyl groups. The O3 peak at 532.1 eV relates with the defect sites lacking of oxygen coordination. The O4 peak at 533.2 eV corresponds to the multiplicity of physi/chemisorbed water on the surface.[42] Among the surface elements, carbon has the highest atomic proportion which proves CDs mainly locate on the material surface. As Figure S5E (Supporting Information) shows, the C 1s curve can be divided into three parts, including the C=C groups or C−H (BE = 285.3 eV), C−O groups and/or C−N (BE = 586.7 eV), and O=C−O groups (BE = 289.2 eV).[43] The above XPS data

prove that CDs mainly locate on the surface of CDs/$NiCo_2O_4$ composites and carry abundant organic functional groups. In addition, the XPS data show carbon has the highest ratio among the elements on the composite surface, which means a lot of CDs coating around $NiCo_2O_4$. Such structure has two main benefits in sensitization and protection. On one hand, CDs facilitate the ion diffusion and charge transport kinetics,[7] which are required for the high-rate application. On the other, CDs can suppress the dissolution and agglomeration of the $NiCo_2O_4$,[8] which is particularly important for long-term cycles. Therefore, such structure can improve the whole performances of the composite materials.

Cyclic voltammetry (CV) experiments are carried out at various sweep rates to examine the redox processes of the $NiCo_2O_4$ and CDs/$NiCo_2O_4$ composites (see **Figure 2**A and Figure S6 (Supporting Information)). A couple of redox peaks are observed within 0.25–0.55 V versus Hg/HgO (reference solution is 1 mol L^{-1} KOH solution). These peaks correspond to the extraction and the insertion of protons, respectively, and can be interpreted by the following equations[44]

$$NiCo_2O_4 + OH^- + H_2O \leftrightarrow NiOOH + 2CoOOH + e^- \quad (1)$$

$$CoOOH + OH^- \leftrightarrow CoO_2 + H_2O + e^- \quad (2)$$

For NCO-0.25, the linear relationship of the anodic peak current density versus $v^{1/2}$ in Figure 2B suggests a diffusion-controlled reaction for the redox reaction of the composites, and this result coincides with the electrode reaction type of $NiCo_2O_4$ based materials.[45–47]

Electrochemical impedance spectroscopy (EIS) is employed to study the capacitive behavior of CDs/$NiCo_2O_4$ composites in another way. In a typical Nyquist impedance plot like Figure 2C, the semicircle at the high-frequency region reflects the conductivity of the electrode materials and electrolyte. The curve in the high-to-medium-frequency region shows the charge transfer resistance which is related with the nature of the material and the combination between the material and the current collector.[39] The nearly vertical line along the imaginary axis at the low-frequency region depends on the capacitive features.[31] At the high and medium frequency regions as shown in the inset of Figure 2C, the semicircles are extended to intersect with the X axis to obtain the fitted radius of the semicircles. For the samples NCO-0, NCO-0.25, NCO-0.5, and NCO-1, the fitted values are 0.133, 0.122, 0.069, and 0.070 Ω, respectively, which are considered as the internal contact resistances of the electrodes (R_{ct}). And this trend suggests that CDs make a positive effect on decreasing the electrochemical impedance of the materials.[7] It is well known that the Nyquist plot of an ideal electrode material at the low frequency region is a vertical line, and the more vertical the line, the better capacitive performance it represents.[31] Among the results of these electrode materials, the slope of $NiCo_2O_4$ plot is significantly smaller than those of the nanocomposites, indicating that the electrodes made of CDs/$NiCo_2O_4$ composites will perform better.

Galvanostatic charge–discharge (GCD) tests are employed to investigate the electrochemical capacitive performances of our products (Figure S7, Supporting Information). At different current densities, every discharge time is

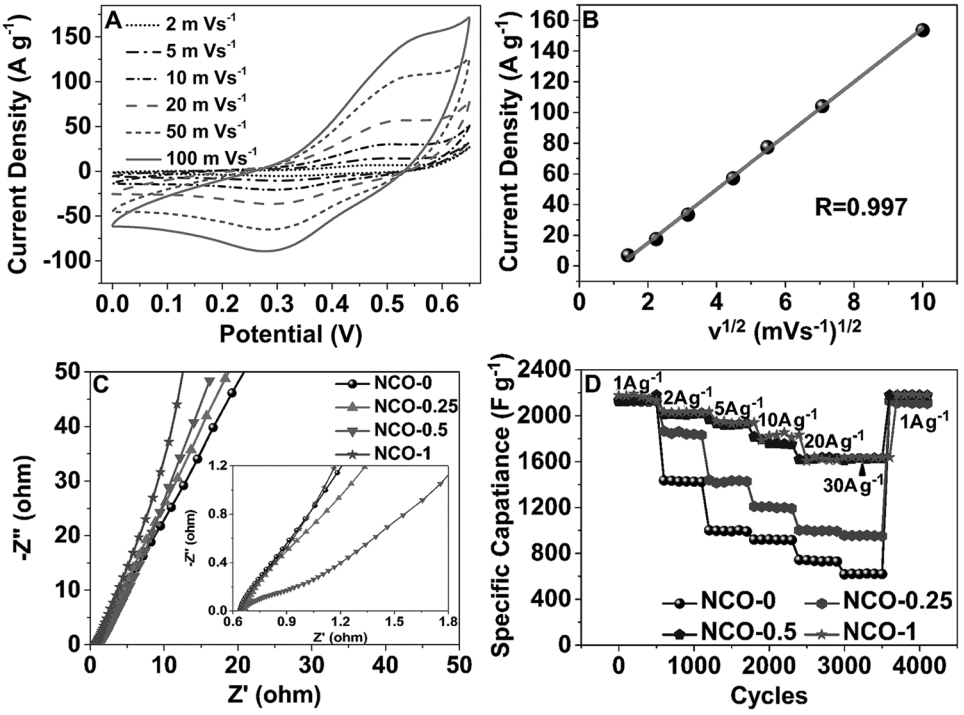

Figure 2. A) CV curves of NCO-0.5 at different scan rates, and B) the relationship between current density and (v = scan rate)$^{1/2}$. C) Nyquist impedance plots of CDs/$NiCo_2O_4$ composites at the open-circuit potential. D) Cycling stability and rate performances of the different samples at various current densities.

equal to the charging time for all GCD curves. And there is no obvious ohmic drop for all discharge curves. The optimal capacitance of NCO-0.5 reaches 2168 F g^{-1} at 1 A g^{-1}, which is calculated by the equation

$$C_m = It/m\Delta V \quad (3)$$

C_m is the specific capacitance, I is the current, t is the discharge time, m is the mass of active materials, and ΔV is the discharge voltage. Figure 2D shows the variation of the specific capacitance and the cycling stability for different materials at current densities from 1 to 30 A g^{-1}. Free $NiCo_2O_4$ has a good cycling stability, but its retention rate is only 29.5%. After incorporation with CDs, NCO-0.5 and NCO-1 exhibit retention rates of 75.2% and 74.4%, respectively, which are superior over the retention rate of the single-crystalline $NiCo_2O_4$[46] (47.0% at current density of 1–8 A g^{-1}) and that of the $NiCo_2O_4$-$MnCo_2O_4$ composite[48] (69.1% at current density of 1–10 A g^{-1}). It should be mentioned that the optimal NCO-0.5 sample also exhibits an excellent cycling stability. In Figure S8 (Supporting Information), after 10 000 cycles, its capacity decay rates are only 3.5% at 5 A g^{-1}, 0.4% at 10 A g^{-1}, 0.5% at 20 A g^{-1}, and 0.3% at 30 A g^{-1}, respectively.

Such remarkable electrochemical performances of our CDs/$NiCo_2O_4$ composites result from the unique structures with three major advantages (**Scheme 2**). First, the high SSA and mesoporous architecture of the composites increase the interface area of the electrode/electrolyte and provide more active sites for electrochemical reactions.[49] Second, the surface structures of the composite spheres facilitate ion diffusion and electron transport, which benefit the rate performances of the composites. In comparison with nanoneedles (150 nm in diameter for urchin NCO-0 and 70 nm in diameter for chestnut NCO-0.25), the nanopetals on NCO-0.5 (ca. 30 nm in thickness) and the nanodots on NCO-1 (ca. 30 nm in diameter) provide the shorter path for the carrier transfer, so that the latter two samples exhibit the better rate performances. Third, all of the four structures are beneficial to relax the volume expansion and relieve the structure damage during cyclings.[49]

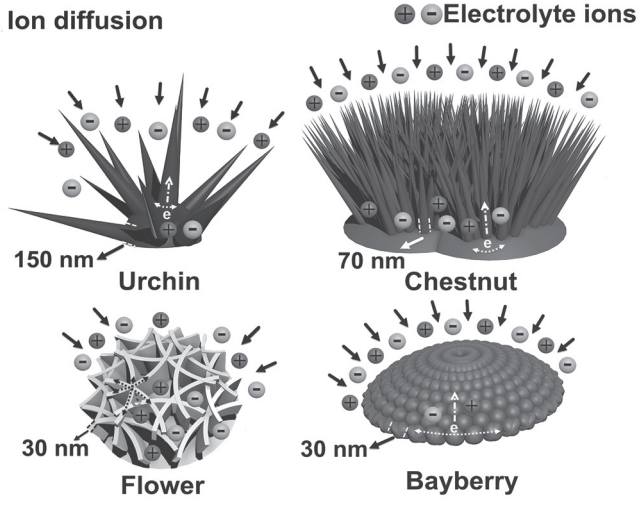

Scheme 2. Simulation of ion diffusion on the material surfaces.

To evaluate the as-prepared CDs/$NiCo_2O_4$ materials for practical applications, a hybrid supercapacitor is fabricated by using NCO-0.5 as the positive electrode and HPC as the negative electrode, respectively. According to our previous work about HPC materials,[31] the mass ratio of the positive electrode to the negative electrode is set to be 0.2 for the charge balance. **Figure 3**A shows the CV curves of the asymmetric supercapacitor at various scan rates in a potential range of 0–1.5 V. The oxidation and reduction peaks of the CV curves can be observed, showing a typical redox reaction behavior.[15] In order to further illustrate the electrochemical properties of the asymmetric capacitor, GCD curves at various current densities are illustrated in Figure 3B. The specific capacitance (C_m) based on the total mass of the active materials of the two electrodes is calculated by the Equation (3), where m is the total mass of two electrodes. The maximum specific capacitance is calculated to be 138.8 F g^{-1} at a current density of 1 A g^{-1}. It should be mentioned that each discharge curve is nearly symmetric with its charge curve, indicating an excellent electrochemical reversibility and a good coulombic efficiency.[2] More importantly, the HPC//NCO-0.5 device reveals good rate capability with a capacitance retention of 61.1% even at a high current density of 30 A g^{-1} (Figure 3C). Figure 3D shows the cycling performance of the device at various current densities. After 5000 cycles, the capacity decays are only 0.10% at 5 A g^{-1}, 0.08% at 10 A g^{-1}, 0.05% at 20 A g^{-1}, and 0.04% at 30 A g^{-1}, respectively, indicating the excellent cycle durability of the optimal HPC//NCO-0.5 hybrid supercapacitor.

Power density and energy density are the key parameters to judge the performance and predict the application of a supercapacitor. According to the Equation (4)

$$E = QV/m \quad (4)$$

where E is the energy density, Q is the quantity of electric charge, V is the average discharge voltage, and m is the total weight of cathode and anode materials, respectively, and the Equation (5)

$$P = IV/m \quad (5)$$

where P is the power density, I is the applied current, and V is the average discharge voltage, respectively, the Ragone plots of HPC//NCO-0.5 (**Figure 4**) are derived from the discharge curves in Figure 3B. This hybrid supercapacitor delivers an energy density of 62.0 Wh kg^{-1} at a power density of 216.0 W kg^{-1}, and it still delivers an energy density of 37.6 Wh kg^{-1} even at a high power density of 6.4 kW kg^{-1}. Such performances are superior over many other $NiCo_2O_4$ systems like carbon-nanotubes@$NiCo_2O_4$//activated carbon (AC),[21] $NiCo_2O_4$@Au-nanotubes//AC,[25] $NiCo_2O_4$-MnO_2// activated graphene (AG),[26] $NiCo_2O_4$//AC,[50] and also graphene quantum dots/$NiCo_2O_4$//AC[2] hybrid capacitors. For practical applications, the leakage current and the self-discharge of a supercapacitor should be minimized, and these data of our asymmetric supercapacitors are shown in Figure S9 (Supporting Information). The leakage current of the hybrid supercapacitor was measured by keeping the

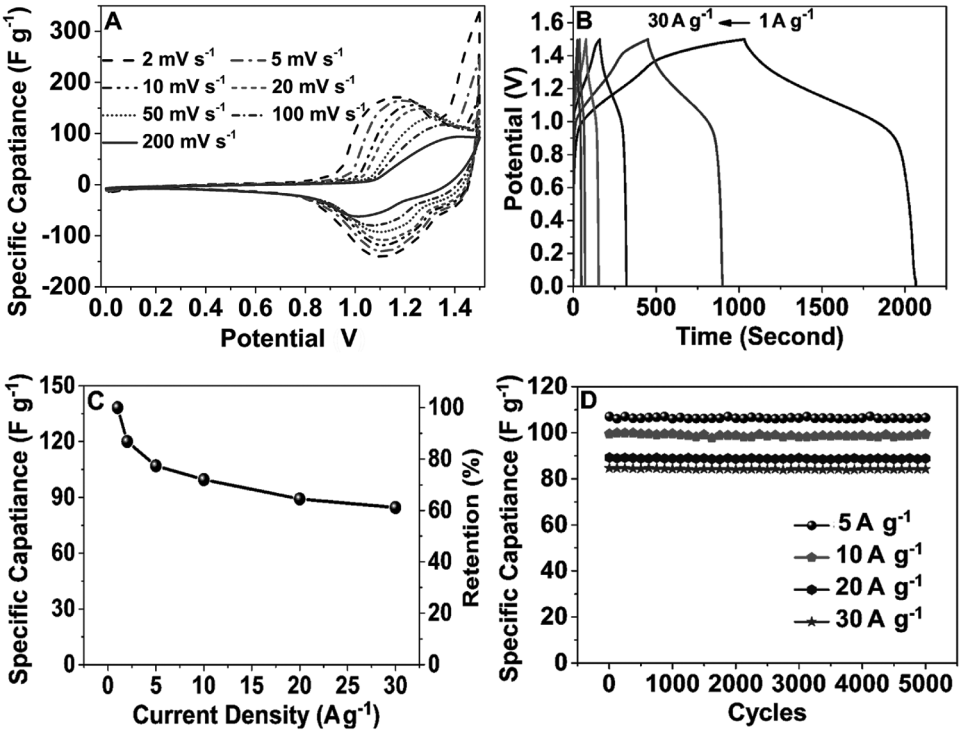

Figure 3. A) CV curves of the hybrid supercapacitor at scan rates of 2–100 mV s^{-1}. B) GCD curves of the hybrid supercapacitor at current densities of 1–30 A g^{-1}. C) Rate performances and D) cycle stability of the hybrid supercapacitor at various current densities.

device at a constant voltage of 1.5 V, after being charged at a constant current of 1.5 mA. As shown in Figure S9A (Supporting Information), the leakage current falls rapidly from 0.5 to 0.1 mA after 120 s and then gradually becomes stable at ≈50 μA for a long time. The self-discharge curve (Figure S9B, Supporting Information) of our supercapacitor device was obtained by precharging it to 1.5 V immediately and detecting the self-discharge within a long time of 24 h. The device exhibited an open circuit voltage of ≈1.0 V after 3 h, and then the voltage drop was only 0.30 V in the next period of 21 h.

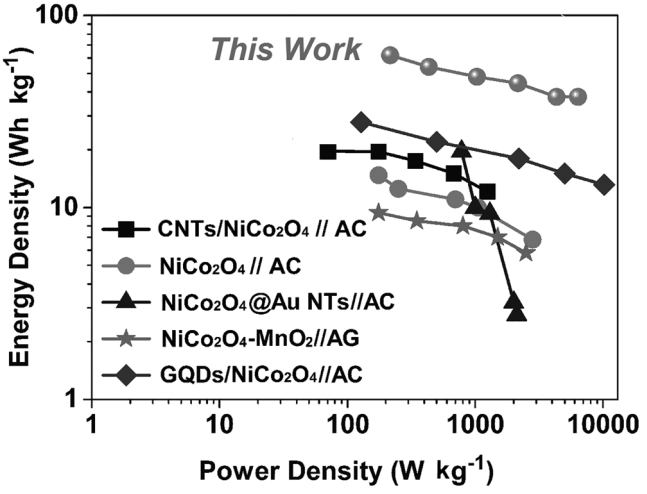

Figure 4. Ragone plots of our NCO-0.5//HPC device and other $NiCo_2O_4$ based supercapacitors reported previously.

In summary, CDs/$NiCo_2O_4$ nanocomposites with various morphologies are successfully prepared by a facile one-step hydrothermal route and a subsequent calcination treatment. All composites manifest excellent capacity performances and cycling stabilities. Among them, NCO-0.5 and NCO-1 exhibit superior rate properties. In addition, a hybrid supercapacitor based on NCO-0.5 and HPC presents both a high energy density and a high power density, and exceptional cycling stability over 5000 cycles at different current densities. These outstanding performances are credited to the CDs, which have played key roles in the supercapacitors. First, the high power density and rate capability of the supercapacitor depend on the fast ions diffusion and redox reactions, which are accelerated by the small sizes and 0D of CDs. Second, the high specific capacitance and energy density are based on the reversible redox reactions of $NiCo_2O_4$, which are facilitated by the good wettability and low electrochemical impedance of CDs/$NiCo_2O_4$ composites, and these advantages are undoubtedly due to the highly graphitized cores and the abundant surface groups of CDs. Finally, the excellent cycling stability relies on the stable electrochemical reactions and the suppressed volume changes, which are benefited from the uniform surface states and homogeneous distribution of CDs in composites. Therefore, we believe CDs will make a great contribution to the electrochemical energy storage in the future.

Experimental Section

Synthesis of N Doped CDs: 0.1 g of anhydrous CA, 300 μL of EDA, and 0.2 g of P_2O_5 were added into a Teflon-lined stainless

steel autoclave, followed by the addition of 500 µL of water. The sealed autoclave was heated at 110 °C for 4 h. After cooling down to room temperature, 5 mL of water was added into the reactants to form a clear solution. The CDs were obtained by adding ethanol into the solution and collecting the precipitate after centrifugation. The precipitate was washed by ethanol and further dried in a vacuum oven at 40 °C for 24 h. The product (CDs) was brown powder with a yield of 70%–75%.

Synthesis of CDs/$NiCo_2O_4$ on Ni Foam: For the synthesis of CDs/$NiCo_2O_4$ composites, 1 mmol of $Ni(NO_3)_2{\cdot}6H_2O$, 2 mmol of $Co(NO_3)_2{\cdot}6H_2O$, and different amounts of CDs powder (0, 10, 20, and 40 mg) were dissolved into a mixed solution of 20 mL of ethanol and 20 mL of H_2O at room temperature to form a clear pink solution, followed by the addition of 12 mmol of urea. The solution was continuously stirred for 10 min and then transferred into a 50 mL Teflon-lined stainless steel autoclave. The rectangular Ni foam (1 cm × 2 cm) was immersed in 2 mol L^{-1} of HCl acetone solution and cleaned ultrasonically for 15 min to get rid of the possible surface oxide layer before it was put into the autoclave for reaction. After reaction for 8 h at 90 °C, the autoclave was cooled down to the room temperature naturally, then the Ni foam was cleaned by ultrasonication to remove the loosely attached products on the surface before drying at 60 °C for 12 h in an oven. The Ni foam with the as-grown precursor was annealed at 250 °C in air atmosphere for 120 min with a slow heating rate of 1 °C min^{-1}. The loading mass of active materials on each Ni foam piece (2 cm^2) was around 1.5 mg, which was calculated by weighting the foam after calcination. These products were denoted as NCO-*X*, in which *X* was 0, 0.25, 0.5, and 1, respectively, representing the concentrations (mg mL^{-1}) of CDs added in the reaction.

Electrochemical Measurements: All the electrochemical tests were conducted with a CH Instruments 660E electrochemical workstation and a CT2001A Land cell tester in a 3 mol L^{-1} of aqueous KOH electrolyte with a three-electrode cell system. A stainless steel grid with activated carbon film, which was prepared by pressing a mixture of the activated carbon (75 wt%), acetylene black (20 wt%), and polytetrafluoroethylene binder (5 wt%) onto a stainless steel grid with an area of 3 cm^2, served as the counter electrode and Hg/HgO (in 1 mol L^{-1} of KOH solution) served as the reference electrode. CV was recorded at the potential range of 0–0.65 V and the scan rate was set from 2 to 100 mV s^{-1}. GCD tests were performed at the potential range of 0–0.47 V, while the current densities varied from 1 to 30 A g^{-1}. The frequency limits of EIS measurements were set at 100 kHz–0.01 Hz with 5 mV of voltage amplitude at the open-circuit potential. The hybrid supercapacitor was fabricated by using the CDs/$NiCo_2O_4$ composite (NCO-0.5) as the positive electrode, HPC as the negative electrode, and 3 M of KOH solution as the electrolyte. The HPC was prepared by referring to our previous research.[31] The preparation of the negative electrode was the same as that of the counter electrode in a three-electrode cell system. The mass ratio of the positive electrode versus the negative electrode was about 1:4 to ensure the same capacity of the positive electrode as that of the negative one. The CV and GCD tests of the hybrid supercapacitor were also performed on a CH Instruments 660E electrochemical workstation and a CT2001A Land cell tester. CV tests were recorded at the potential range of 0–1.50 V and the scan rate was set from 2 to 100 mV s^{-1}. GCD tests were also performed at the potential range of 0–1.50 V, while the current densities varied from 1 to 30 A g^{-1}.

Supporting Information

Supporting Information is available from the Wiley Online Library or from the author.

Acknowledgements

This work was supported by the National Major Basic Research Program of China (2013CB934101), the National Natural Science Foundation of China (21271045), and NCET-11-0115.

[1] Y. Zhu, X. Ji, C. Pan, Q. Sun, W. Song, L. Fang, Q. Chen, C. E. Banks, *Energy Environ. Sci.* **2013**, *6*, 3665.
[2] Y. Zhu, Z. Wu, M. Jing, H. Hou, Y. Yang, Y. Zhang, X. Yang, W. Song, X. Jia, X. Ji, *J. Mater. Chem. A* **2015**, *3*, 866.
[3] W. W. Liu, Y. Q. Feng, X. B. Yan, J. T. Chen, Q.-J. Xue, *Adv. Funct. Mater.* **2013**, *23*, 4111.
[4] W. Liu, X. Yan, J. Chen, Y. Feng, Q. Xue, *Nanoscale* **2013**, *5*, 6053.
[5] C. Ding, A. Zhu, Y. Tian, *Acc. Chem. Res.* **2014**, *47*, 20.
[6] S. N. Baker, G. A. Baker, *Angew. Chem., Int. Ed.* **2010**, *49*, 6726.
[7] X. Li, M. Rui, J. Song, Z. Shen, H. Zeng, *Adv. Funct. Mater.* **2015**, *25*, 4929.
[8] D. Chao, C. Zhu, X. Xia, J. Liu, X. Zhang, J. Wang, P. Liang, J. Lin, H. Zhang, Z. X. Shen, H. J. Fan, *Nano Lett.* **2015**, *15*, 565.
[9] L. Lv, Y. Fan, Q. Chen, Y. Zhao, Y. Hu, Z. Zhang, N. Chen, L. Qu, *Nanotechnology* **2014**, *25*, 235401.
[10] M. Hassan, E. Haque, K. R. Reddy, A. I. Minett, J. Chen, V. G. Gomes, *Nanoscale* **2014**, *6*, 11988.
[11] X. Wei, S. Wan, X. Jiang, Z. Wang, S. Gao, *ACS Appl. Mater. Interfaces* **2015**, *7*, 22238.
[12] X. Wei, X. Jiang, J. Wei, S. Gao, *Chem. Mater.* **2016**, *28*, 445.
[13] Y. Wang, Y. Xia, *Adv. Mater.* **2013**, *25*, 5336.
[14] Y. Zhai, Y. Dou, D. Zhao, P. F. Fulvio, R. T. Mayes, S. Dai, *Adv. Mater.* **2011**, *23*, 4828.
[15] M. Salanne, B. Rotenberg, K. Naoi, K. Kaneko, P. L. Taberna, C. P. Grey, B. Dunn, P. Simon, *Nat. Energy* **2016**, *1*, 16070.
[16] P. Simon, Y. Gogotsi, B. Dunn, *Science* **2014**, *343*, 1210.
[17] D. P. Dubal, P. Gomez-Romero, B. R. Sankapal, R. Holze, *Nano Energy* **2015**, *11*, 377.
[18] V. Gupta, S. Gupta, N. Miura, *J. Power Sources* **2010**, *195*, 3757.
[19] A. V. Chadwick, S. L. P. Savin, S. Fiddy, R. Alcántara, D. F. Lisbona, P. Lavela, G. F. Ortiz, J. L. Tirado, *Phys. Chem. C* **2007**, *111*, 4636.
[20] B. Dong, X. Zhang, X. Xu, G. Gao, S. Ding, J. Li, B. Li, *Carbon* **2014**, *80*, 222.
[21] F. Cai, Y. Kang, H. Chen, M. Chen, Q. Li, *J. Mater. Chem. A* **2014**, *2*, 11509.
[22] J. Hu, M. Li, F. Lv, M. Yang, P. Tao, Y. Tang, H. Liu, Z. Lu, *J. Power Sources* **2015**, *294*, 120.
[23] M. F. L. De Volder, S. H. Tawfick, R. H. Baughman, A. J. Hart, *Science* **2013**, *339*, 535.
[24] G. Q. Zhang, H. B. Wu, H. E. Hoster, M. B. Chan-Park, X. W. Lou, *Energy Environ. Sci.* **2012**, *5*, 9453.
[25] J. Zhu, Z. Xu, B. Lu, *Nano Energy* **2014**, *7*, 114.
[26] M. Kuang, Z. Q. Wen, X. L. Guo, S. M. Zhang, Y. X. Zhang, *J. Power Sources* **2014**, *270*, 426.
[27] H. Ding, H. M. Xiong, *RSC Adv.* **2015**, *5*, 66528.
[28] H. Ding, J. S. Wei, H. M. Xiong, *Nanoscale* **2014**, *6*, 13817.
[29] H. Ding, S. B. Yu, J. S. Wei, H. M. Xiong, *ACS Nano* **2016**, *10*, 484.
[30] S. Gao, Y. Chen, H. Fan, X. Wei, C. Hu, L. Wang, L. Qu, *J. Mater. Chem. A* **2014**, *2*, 6320.

[31] J. S. Wei, H. Ding, Y. G. Wang, H. M. Xiong, *ACS Appl. Mater. Interfaces* **2015**, *7*, 5811.
[32] V. Thirumal, A. Pandurangan, R. Jayavel, K. S. Venkatesh, N. S. Palani, R. Ragavan, R. Ilangovan, *J. Mater. Sci: Mater. Electron.* **2015**, *26*, 6319.
[33] H. Xu, J. X. Wu, Y. Chen, J. L. Zhang, B. Q. Zhang, *Ionics* **2015**, *21*, 2615.
[34] A. K. Das, R. K. Layek, N. H. Kim, D. Jung, J. H. Lee, *Nanoscale* **2014**, *6*, 10657.
[35] Y. Wang, J. He, C. Liu, W. H. Chong, H. Chen, *Angew. Chem., Int. Ed.* **2015**, *54*, 2022.
[36] J. Xiao, S. Yang, *RSC Adv.* **2011**, *1*, 588.
[37] Y. Fan, L. Wang, J. Li, J. Li, S. Sun, F. Chen, L. Chen, W. Jiang, *Carbon* **2010**, *48*, 1743.
[38] J. Du, G. Zhou, H. Zhang, C. Cheng, J. Ma, W. Wei, L. Chen, T. Wang, *ACS Appl. Mater. Interfaces* **2013**, *5*, 7405.
[39] D. Cai, S. Xiao, D. Wang, B. Liu, L. Wang, Y. Liu, H. Li, Y. Wang, Q. Li, T. Wang, *Electrochim. Acta* **2014**, *142*, 118.
[40] H. Chen, J. Jiang, L. Zhang, Y. Zhao, D. Guo, Y. Ruan, D. Xia, *ChemPlusChem* **2015**, *80*, 181.
[41] L. Shen, Q. Che, H. Li, X. Zhang, *Adv. Funct. Mater.* **2014**, *24*, 2630.
[42] N. Garg, M. Basu, A. K. Ganguli, *J. Phys. Chem. C* **2014**, *118*, 17332.
[43] S. H. Tamboli, B. S. Kim, G. Choi, H. Lee, D. Lee, U. M. Patil, J. Lim, S. B. Kulkarni, S. Chan Jun, H. H. Cho, *J. Mater. Chem. A* **2014**, *2*, 5077.
[44] Z. Wu, Y. Zhu, X. Ji, *J. Mater. Chem. A* **2014**, *2*, 14759.
[45] T. Brousse, D. Belanger, J. W. Long, *J. Electrochem. Soc.* **2015**, *162*, A5185.
[46] C. An, Y. Wang, Y. Huang, Y. Xu, L. Jiao, H. Yuan, *Nano Energy* **2014**, *10*, 125.
[47] Y. Wang, D. Zhou, D. Zhao, M. Hou, C. Wang, Y. Xia, *J. Electrochem. Soc.* **2012**, *160*, A98.
[48] Y. Zhai, H. Mao, P. Liu, X. Ren, L. Xu, Y. Qian, *J. Mater. Chem. A* **2015**, *3*, 16142.
[49] X. Y. Yu, X. Z. Yao, T. Luo, Y. Jia, J. H. Liu, X. J. Huang, *ACS Appl. Mater. Interfaces* **2014**, *6*, 3689.
[50] R. Ding, L. Qi, M. Jia, H. Wang, *Electrochim. Acta* **2013**, *107*, 494.

Received: June 30, 2016
Revised: August 20, 2016
Published online: September 26, 2016